Geochemical Perspectives Letters

Isotopic evidence of sulfur photochemistry during lunar regolith formation

J.W. Dottin III, J. Farquhar, S.-T. Kim, C. Shearer, B. Wing, J. Sun, P. Ni

Supplementary Information

The Supplementary Information includes:

- Supplementary Tables S-1 and S-2
- Supplementary Text S-1. Detailed Methods
- Supplementary Text S-2. Sulfur Loss Models
- Supplementary Text S-3. Isotopic Discrepancy Between Lunar Soils and Basalts
- Additional Supplementary Figures S-6 and S-7
- Supplementary Information References

Supplementary Tables

Table S-1 Sulfur isotope compositions and sulfur concentrations of lunar soils and glasses. Abbreviation n.d. denotes not detected. Our uncertainties on $\delta^{34}S$, $\Delta^{33}S$, and $\Delta^{36}S$ are estimated as ±0.3, ±0.008, and ±0.3 ‰ respectively (all 2σ) from long-term reproducibilities on measurements of standards. †Our uncertainty on $\Delta^{33}S$ for the <10 μm size fraction in sample 75081, 690 is 0.016 ‰ (2σ) due to small sample size.

Sample	Sieve size (μm)	Mass digested (g)	S (ppm)	$\delta^{34}S$ (‰)	$\Delta^{33}S$ (‰)	$\Delta^{36}S$ (‰)
74241, 204	0–10	0.4491	1268	7.29	0.003	0.48
	10–20	0.4491	1196	4.50	0.001	0.34
	20–45	0.512	726	3.22	−0.003	0.27
	45–75	0.3968	804	2.72	0.001	0.18
	75–90	0.131	762	3.29	−0.014	0.29
	90–150	0.3641	864	2.49	−0.006	0.14
	150–250	0.2776	834	2.15	−0.014	0.11
	250–500	0.2563	976	1.81	−0.011	0.10
	500–1000	0.1841	1157	1.59	−0.017	0.11

Table S-1 continued.

Sample	Sieve size (µm)	Mass digested (g)	S (ppm)	$\delta^{34}S$ (‰)	$\Delta^{33}S$ (‰)	$\Delta^{36}S$ (‰)
75081, 690	0–10	0.0117	1725	9.91	−0.163†	1.44
	10–20	0.1593	1724	6.26	−0.089	0.58
	20–45	0.3525	1055	6.01	−0.043	0.31
	45–75	0.4346	815	4.60	−0.047	0.38
	75–90	0.0992	549	4.12	−0.070	0.75
	90–150	0.4526	722	3.63	−0.029	0.33
	150–250	0.3825	856	2.76	−0.031	0.27
	250–500	0.325	922	2.36	−0.041	0.21
	500–1000	0.1654	1130	1.69	−0.024	0.15
	>1000	0.0039	n.d.			

Table S-2 Petrography of lunar soils analysed.

Components	74241	75081
Agglutinates	8	35.3
Basalt	30	19.7
Breccia	16.9	3.4
Anorthosite	0.6	0.3
Norite	-	-
Gabbro	-	-
Plagioclase	4.6	9
Pyroxene	11.3	20.3
Olivine	-	0.7
Ilmenite	1.3	5.7
Orange glass	4	0.7
Glass other	22.5	4.9

All values are in wt. %. Data are from Heiken and McKay (1974).

Supplementary Text S-1. Detailed Methods

Samples 74241, 204 and 75081, 690 were sieved in 9 and 10 grain size fractions, respectively. The smallest grain sizes were sieved with HFE-7100 3M Novec fluid. All fluid was evaporated with sieved fraction. For 74241, 204 and 75081, 690, sulfur was extracted using an HF + $CrCl_2$ digestion method described in (Dottin *et al.*, 2021). Each sieved sample was placed into a Teflon reaction vessel with a stir bar and attached to a water trap and an $AgNO_3$ trap. This set up was purged for 10–15 minutes prior to injection of 20 mL of an acidic chromium (II) chloride solution, 10 mL of hydrochloric acid, and 10 mL of hydrofluoric acid. The sample + acid bath was then heated to ~70 °C and stirred while allowing N_2 to continuously flow through the setup. Sulfur was released from the sample as H_2S and first carried through a water trap (to trap acid) and subsequently into an $AgNO_3$ trap, where sulfur was precipitated as Ag_2S. We allowed this reaction to run for ~2.5 to 3 hours.

After sitting in the dark for at least one week, precipitated Ag_2S was rinsed with Milli-Q water six times, dried at 70 °C for ~2 hours, and weighed to estimate sulfur concentration in the sample. Weighed Ag_2S was then placed into foil packets and reacted with ~10× excess fluorine to produce SF_6. The purification of product SF_6 follows the methods described in (Dottin *et al.*, 2021) closely. Briefly, SF_6 is first frozen into a liquid nitrogen cooled trap and excess F_2 is passivated using a heated KBr salt. Following passivation, the remaining SF_6 is subjected to an ethanol slush at around −111 °C where it is separated from additional contaminants, such as HF (produced during the fluorination). The separated SF_6 is then injected into a gas chromatograph for a final purification and trapped using liquid nitrogen cooled coils. The purified SF_6 was lastly analysed using a ThermoFinnigan MAT 253 dual inlet isotope ratio mass spectrometer. Isotopic analyses of the purified SF_6 are performed by monitoring SF_5^+ ion beams at m/z of 127, 128, 129, and 131. Isotopic data are reported in per mil using the following notation:

$$\delta^{34}S = [(({}^{34}S/{}^{32}S)_{sample} / ({}^{34}S/{}^{32}S)_{CDT}) - 1]$$

$$\Delta^{33}S = [(({}^{33}S/{}^{32}S)_{sample} / ({}^{33}S/{}^{32}S)_{CDT}) - (({}^{34}S/{}^{32}S)_{sample} / ({}^{34}S/{}^{32}S)_{CDT})^{0.515}]$$

$$\Delta^{36}S = [(({}^{36}S/{}^{32}S)_{sample} / ({}^{36}S/{}^{32}S)_{CDT}) - (({}^{34}S/{}^{32}S)_{sample} / ({}^{34}S/{}^{32}S)_{CDT})^{1.9}]$$

All samples were bracketed by analyses of internal standard IAEA-S1. All data are first normalised to analyses of IAEA-S1 performed during the analytical sessions and subsequently to a value of IAEA-S1 relative to Canyon Diablo Troilite measurements performed at UMD ($\delta^{34}S = -0.401$ ‰, $\Delta^{33}S = 0.116$ ‰, $\Delta^{36}S = -0.796$ ‰; Antonelli *et al.*, 2014). Uncertainties on $\delta^{34}S$ and $\Delta^{36}S$ (±0.3 ‰) reflect the long-term uncertainty on repeated measurements of IAEA-S1. Uncertainty on $\Delta^{33}S$ reflects mass spectrometry uncertainty associated with counts on ^{33}S and is similar to our long-term uncertainty estimates. Samples analysed three times as 8–26 second cycles on the reference and sample have been attributed a 2σ uncertainty of ±0.016 ‰ and samples analysed nine times as 8–26 second cycles on the reference and sample have been attributed a 2σ uncertainty of ±0.008 ‰. The ability to analyse a sample three or nine times depends on the sample size available for measurements.

Supplementary Text S-2. Sulfur Loss Models

Two models were examined to identify the potential origin for second-order variations in sulfur concentrations seen in the 50–100 μm size fractions.

I. Diffusion and condensation model description

Diffusion for a homogenous 3-D sphere starting at fixed temperature can be described by:

$$\frac{\partial \varphi(\boldsymbol{r},t)}{\partial t} = \nabla \cdot [D(\varphi,\boldsymbol{r})\nabla\varphi(\boldsymbol{r},t)]$$

where $\varphi(\boldsymbol{r},t)$ is the concentration of diffusing element at position $\boldsymbol{r}$ and time t, and $D(\varphi,\boldsymbol{r})$ is the diffusion coefficient for element concentration φ at position $\boldsymbol{r}$ (Crank, 1975). The equation can be simplified if D is a constant to:

$$\frac{\partial \varphi(\boldsymbol{r},t)}{\partial t} = D\nabla^2\varphi(\boldsymbol{r},t).$$

The relationship of D and temperature T for ^{32}S in basalts can be demonstrated with the following equation (Zhang *et al.*, 2010):

$$D^{\text{basalts}}_{^{32}\text{S TD}} = \exp\left[-8.21 - \frac{27{,}692 - 651.6w}{T}\right]$$

where w is wt. % H_2O and 'TD' refers to trace element diffusion.

Diffusion of ^{34}S is evaluated assuming the arbitrary relationship (*e.g.*, Richter *et al.*, 2009):

$$D^{\text{basalts}}_{^{34}\text{S TD}} = \frac{D^{\text{basalts}}_{^{32}\text{S TD}}}{\left(\frac{33.96787}{31.97207}\right)^k}$$

where k is an exponent that varies from 0 to 0.5, which assumes a square root mass relationship. More physically realistic representations for diffusion that rely on diffusion hops through lattice force fields were not explored but should fit within the limits $k = 0 \rightarrow 0.5$.

With initial state conditions, together with a boundary condition that $\varphi(\boldsymbol{r} = a, t)$, this system has an analytical solution of (after Eq. 3-68c in Zhang, 2008):

$$\bar{\varphi}(t,a) = \varphi_0 * \left(1 - \frac{M_t}{M_\infty}\right) = \varphi_0 * \frac{6}{\pi^2}\sum_{n=1}^{\infty}\frac{1}{n^2}e^{-Dn^2\pi^2 t/a^2}$$

where $\bar{\varphi}(t,a)$ is the average concentration at radius a after diffusing for time t. φ_0 is the initial concentration of the homogenous grain, $\frac{M_t}{M_\infty}$ is the proportion of mass loss due to diffusion at time t. Concentration (*i.e.*, $\bar{\varphi}(t,a)$) profiles are calculated for each radius (1–250 μm) grain. A condensed layer added to the outside of each grain follows the model used by (Rees and Thode, 1974) and is used to account for the shift to positive δ^{34}S and higher concentrations of smaller size fractions. The thickness of this layer and the concentrations within this layer are adjusted as in prior studies. One weakness in the diffusion model includes the assumption

of constant temperature and uniform diffusivity since the regolith consists of various minerals, glass, and agglutinates produced by local heating, and the surfaces subject to space weathering. An additional weakness in the model is that it only accounts for isotope effects associated with diffusion and does not account for isotope effects occurring at the edge of the grain by the loss process. These effects could shift the direction of the isotope fractionation.

Adding loss of sulfur via the diffusion model produces a profile of concentrations moving from the grain interiors to the grain edges that scales with grain size and allows the model to reproduce the second order drop in concentration observed for the 50–100 μm size fractions. Inclusion of diffusive isotope fractionation produces a shift to lower $\delta^{34}S$ for the rims but, given the relatively uniform variation in isotope ratios which can be explained by isotopic mixing between an outer layer and a second endmember, fractionations by diffusion and or loss processes are not ruled out by the data, but are not required to reproduce the significant isotopic variations that are seen.

The data reported in Table S-1 fit the *t-T* relationships shown in Figure S-1, which require times that are too long for temperatures that do not involve melting. The possibility of multiple events may exist but would need to compete with comminution by gardening for diffusion to be a viable explanation for the variations in concentration in the 50–100 μm size fractions.

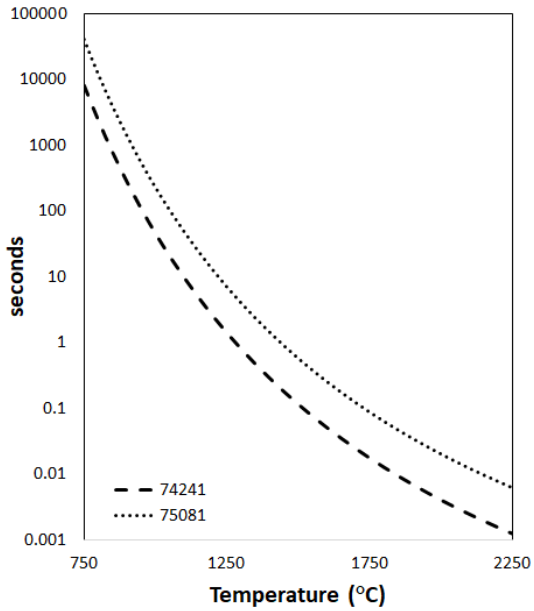

Figure S-1 Diffusivity times related to temperature.

II. The three-layer onion model

The second model invoked a component in addition to the outer layer component and the grain component. For such a component to lead to the concentration deficits seen in the 50–100 μm size fractions, its proportion must increase as particle size decreases. One way to do this is to treat this increase as related to grain surface area and this can be modelled using a simple a three-layer onion model. The inner sphere (Layer 1) is assumed to be unaltered and represents the composition of materials that was hit by the micrometeorite. The depleted shell (Layer 2) is melted and has undergone some sulfur depletion and possible isotope fractionation. Lastly, a condensed outer layer (Layer 3) is added on the surface of the grain. The thickness of the grain follows the model by (Rees and Thode, 1974; Thode and Rees, 1976) that suggests the condensed

layer thickness is between 1 and 3 μm. Fits to this model that also fit the concentration data presented in Table S-1 are reported in Table S-3.

Table S-3 Model fits that match the concentration data presented in Table S-1.

Sample		Inner sphere	Depleted shell	Outer layer
74241, 204	Thickness (μm)		22	2.5
	S concentration (ppm)	1350	600	1300
	S isotopes ($\delta^{34}S$)	1.2	1.2	6
75081, 690	Thickness (μm)		22	2.5
	S concentration (ppm)	1350	275	1750
	S isotopes ($\delta^{34}S$)	1.7	1.7	6

While this result indicates that there is a component with lower sulfur concentration that is more represented in the 50–100 μm size fractions relative to the other grain size fractions, distributing the depleted sulfur component as a second layer around the grains is used just as a possible scaling rule.

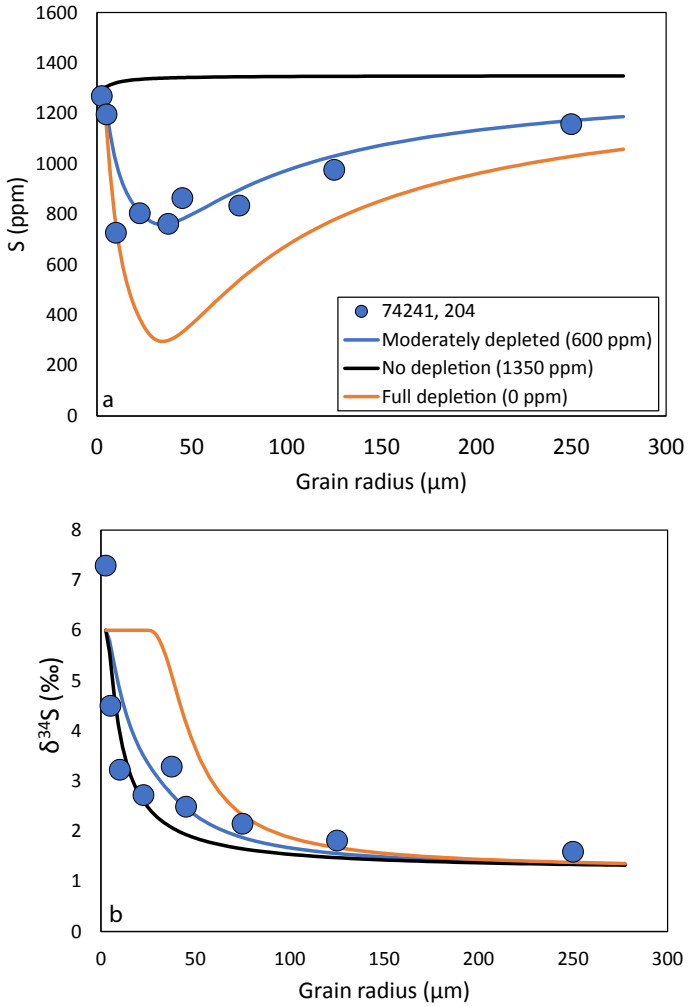

Figure S-2 Example of how our three-layer onion model changes as the concentration of the melt layer is changed. The melt layer is the main factor controlling the behaviour observed among sulfur concentration, sulfur isotopes, and grain size.

III. Evaluating the effect of sulfur escape from the Moon

Our diffusion models suggest no isotopic fractionation during sulfur liberation from a soil grain melting event. Sulfur isotope fractionation associated with sputtering is not well constrained and is likely overprinted by the concomitant fractionation of sulfur loss to space. The process of sulfur loss has several elements. It starts with a process that introduces sulfur species into the atmosphere. Sputtering by solar wind and volatile release from micrometeorite impact melts at temperatures between limits of approximately 1700 K to 3776 K (Cintala, 1992) provide two ways to generate species with high enough energy to exceed the threshold for lunar escape (2380 m/s). In the case of impact melt produced volatiles, it is the higher energy part of the Maxwell-Boltzmann distribution (see following section for details) for ground state atomic sulfur, HS, H_2S, SO, and SO_2 that can escape the lunar gravitational field because mean free paths are very large (hundreds to thousands of kilometers, see following section). The remaining sulfur is enriched in heavy isotopes, and this can be significant for the lightest of these species. The atoms and molecules that do not escape follow ballistic trajectories of hundreds of thousands of km before they return to the surface (see following section). Further, it is not certain whether they will immediately be deposited or ricochet back for

another ballistic arc. At a velocity of 1–2 km/s, these species remain in the atmosphere for hundreds to thousands of seconds on each arc, being distributed across large swaths of the lunar surface. The enhancement of $\delta^{34}S$ for the sulfur fraction that does not escape is calculated for several species as a function of the temperature of the Maxwell-Boltzmann distribution and is shown in Figure S-3.

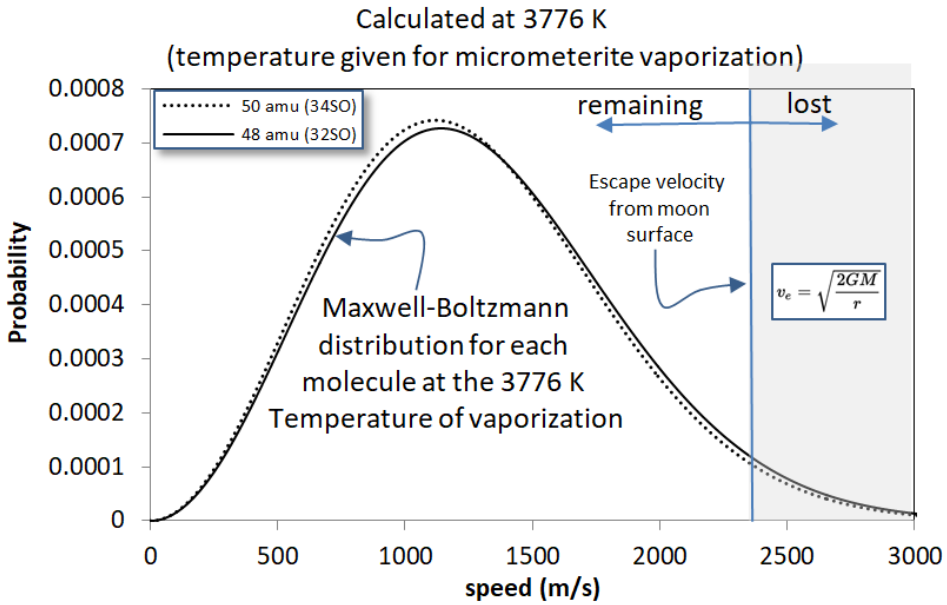

Figure S-3 Maxwell-Boltzmann distribution of SO used to calculated escape velocity on the lunar surface.

IV. Details of atmospheric escape model

The isotopic fractionation associated with loss is calculated using an approach that is similar to that used by Switkowski *et al.* (1977) and Wang *et al.* (2012) (illustrated for loss of SO produced by vaporisation at 3776 K in Fig. S-3).

This approach rests on the assumption that volatile sulfur species acquire a Maxwell-Boltzmann speed distribution set by the temperature at which they are introduced into the lunar atmosphere and then effuse without collisions, either following ballistic trajectories that return them to the lunar surface or escape trajectories that remove them from the Moon. The mean free path of molecules under lunar atmospheric conditions 10^{9}–10^{10} Pa (10^{-15} bar) are on the order of hundreds to thousands of km (Housley *et al.*, 1978). The ballistic trajectories that are calculated are also on this order, but a significant fraction of molecules, more for heavier molecules, are deposited closer to the site of impact because of the 360° × 180° sweep of initial trajectories radiating outward from the point of volatile generation (Fig. S-4).

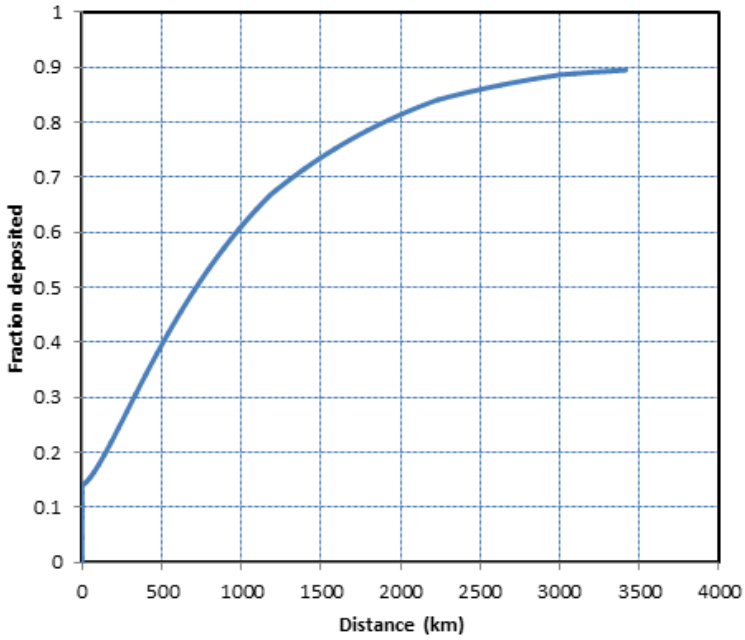

Figure S-4 Calculation of ballistic trajectory of sulfur atoms following azimuthal trajectories at 3776 K.

The temperatures of this process likely fall between the temperature of agglutinate formation and agglutinate evaporation which is assumed to be between 1770 K and 3776 K (Cintala, 1992). The energies of sputtering, a loss process examined by Switkowski *et al.* (1977), are estimated as 1 eV (11,700 K). The volatile species that are produced from typical terrestrial silicate liquids at high temperatures favour formation of atomic sulfur, but also include SO, SO_2, and minor H_2S (Schaefer *et al.*, 2012). Hydrogen-bearing species may be allowed or materials with significant implantation of solar wind. The isotopic fractionations associated with loss are largest for the lightest species. An illustration of the isotopic fractionation imparted on the sulfur that remains after escape is provided in Figure S-5 for temperatures spanning those from Cintala (1992) for vaporisation to those of Switkowski *et al.* (1977) for sputtering.

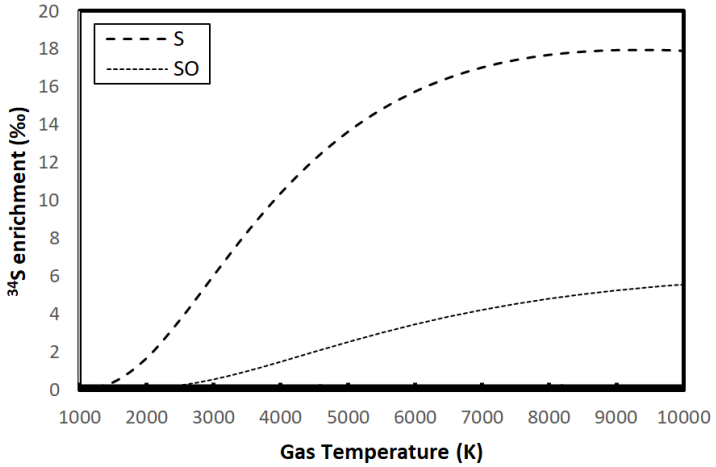

Figure S-5 Sulfur isotope composition of common gaseous sulfur species as a result of fractionation from sulfur escape from the Moon.

Other fractionation processes may also operate. These include isotopic fractionation of species with similar kinetic energy ($E = ½mv^2$) and is approximated by the square root of the ratio of masses [$(m_a/m_b)^{1/2}$], yielding variations between $\delta^{33}S$, $\delta^{34}S$, and $\delta^{36}S$ that scale approximately as 1:2:4 (known as mass-dependent fractionation) and with fractionation factors for $^{34}S/^{32}S$ for species like FeS, SO_2 and SO between 10 and 20 ‰. For this to be effective, the separation of species must be maintained, and homogenisation must not be complete. Studies of diffusive loss and loss into hard vacuum produce ^{32}S enriched residues. Studies of troilite decomposition by McEwing *et al.* (1980) demonstrate that large isotope fractionations can occur, and manifest as depletions in heavy isotopes of the volatilised phase rather than depletions in the light isotopes, as seen in the soils.

Supplementary Text S-3. Isotopic Discrepancy Between Lunar Soils and Basalts

The $\delta^{34}S$ value inferred for grain interiors of our samples (excluding the condensed layer) is shifted to a slightly more positive value (1.2 ‰ to 1.7 ‰) than the average of mare basalts (0.58 ‰; Wing and Farquhar, 2015) Further, the $\delta^{34}S$ value inferred for more mature lunar soils is even higher (Thode and Rees, 1976). These observations indicate that this component either carries a signature acquired during impact gardening or is simply derived from a lunar mantle component like that associated with high-Ti glasses (Saal and Hauri, 2021). If the signature is derived from a gardening event, the data would support reworking of ^{34}S-enriched material as the gardening process continues. An original composition associated with high-Ti mantle melts would have implications for mantle materials that are most broadly distributed across that lunar surface that can be further explored with additional analyses of lunar materials.

Additional Supplementary Figures

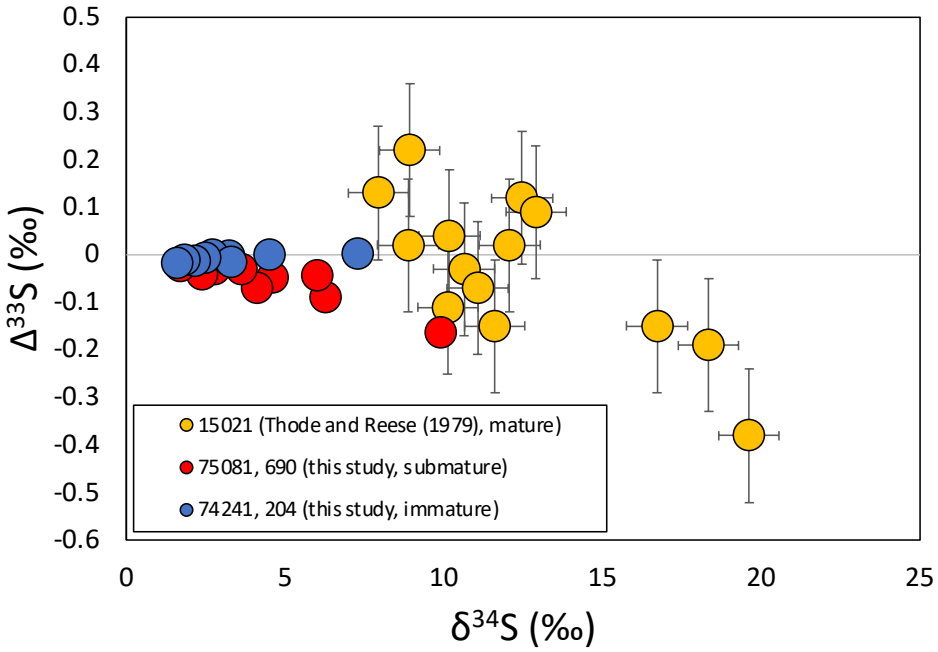

Figure S-6 Sulfur isotope data for 75081, 690-submature (this study) and 15021-mature from (Thode and Rees, 1979) that illustrates potential relationship between $\Delta^{33}S$ and maturity. Uncertainties on data from (Thode and Rees, 1979) are estimated as 2 s.d. on mean of measurements of Canyon Diablo Troilite in (Thode and Rees, 1971). Uncertainties associated with data reported in this study are smaller than the size of the symbols.

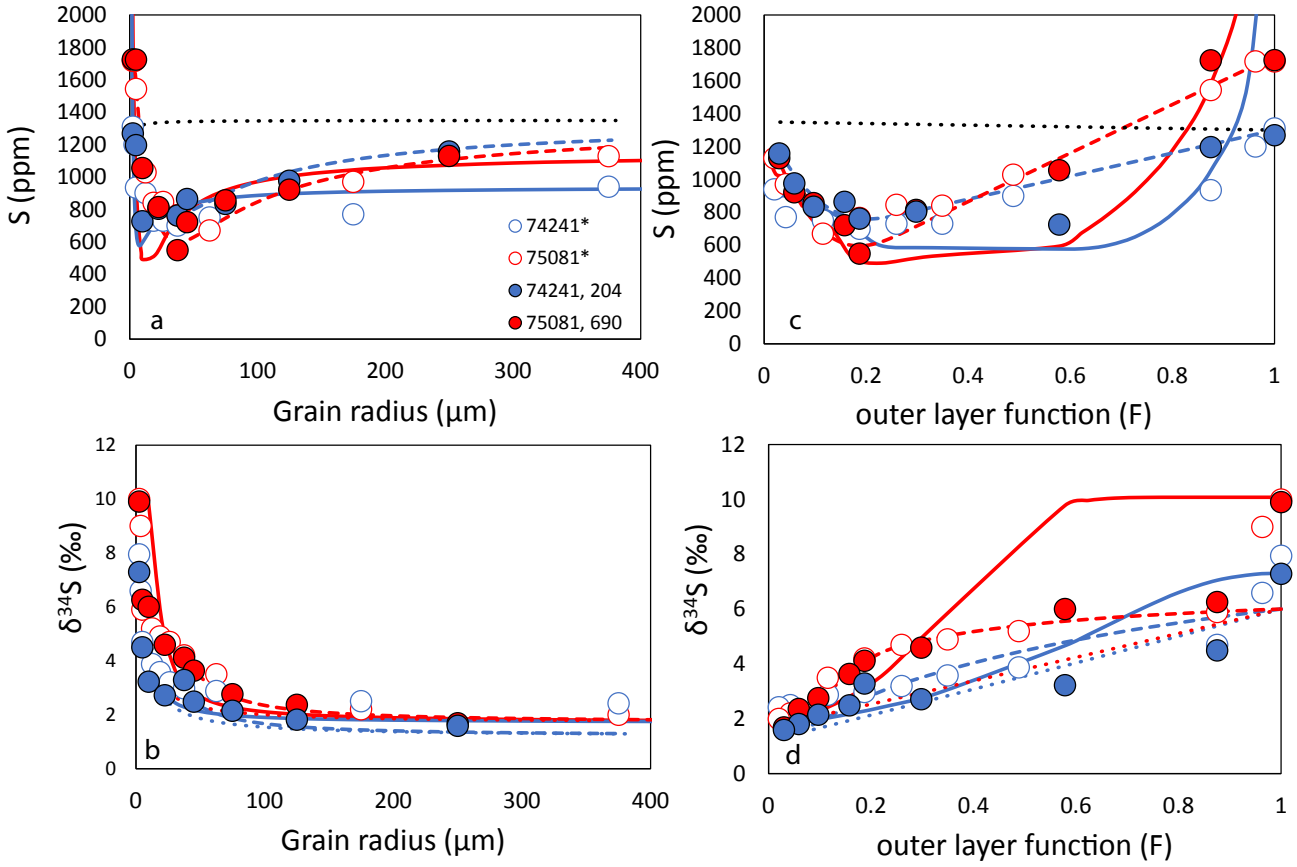

Figure S-7 Sulfur concentration and $\delta^{34}S$ *vs*. the outer layer function (F) and the corresponding grain radius. Data from this study are closed red and blue symbols. Data from Rees and Thode (1974) and Thode and Rees (1976) are shown as open symbols and indicated by * in the legend. $F = \frac{r^3-(r-a)^3}{r^3}$, where r is grain radius and a is the average thickness of the condensed layer, which is set at 1.5 μm (Rees and Thode, 1974). We have also plotted exemplary models for sulfur diffusion (solid red and blue lines). These models are performed at 1200 °C and show the process of diffusion and condensation occurring on integrated timescales of 4 s for 74241, 204 (solid blue line) and 20 s for 75081, 690 (solid red line). We also plot our three-layer model results (dashed lines; see supplementary text for details on parameters). Dotted lines portray the model from Rees and Thode (1974).

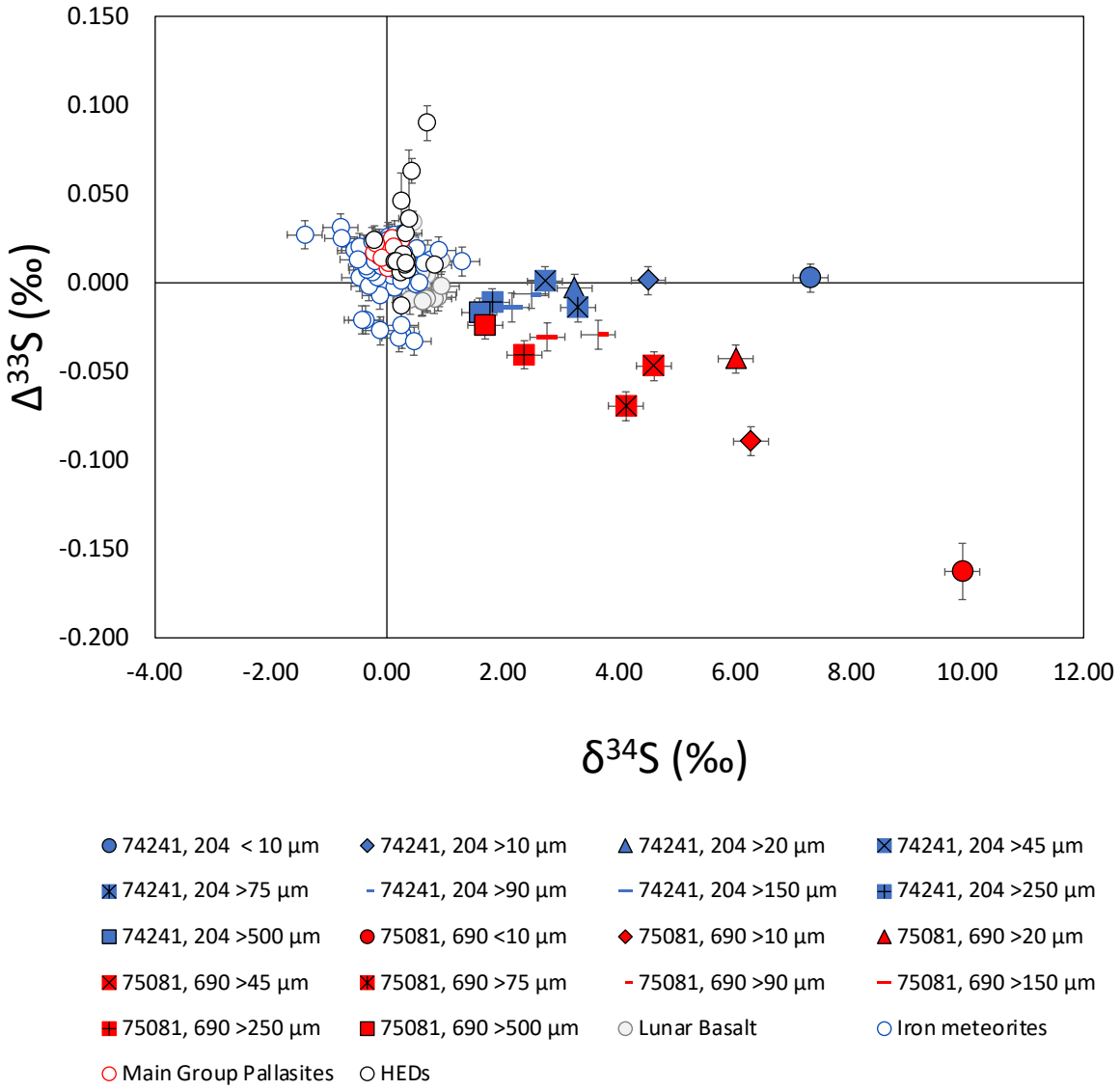

Figure S-8 Sulfur isotope data for lunar soils (this study), lunar basalts (Wing and Farquhar, 2015; Gargano *et al.*, 2022), main group Pallasites (Dottin *et al.*, 2018), iron meteorites (Antonelli *et al.*, 2014), and HED meteorites (Rai *et al.*, 2005; Wu *et al.*, 2018).

Supplementary Information References

Antonelli, M.A., Kim, S.-T., Peters, M., Labidi, J., Cartigny, P., *et al.* (2014) Early inner solar system origin for anomalous sulfur isotopes in differentiated protoplanets. *Proceedings of the National Academy of Sciences* 111, 17749–17754. https://doi.org/10.1073/pnas.1418907111

Cintala, M.J. (1992) Impact-induced thermal effects in the lunar and Mercurian regoliths. *Journal of Geophysical Research: Planets* 97, 947–973. https://doi.org/10.1029/91JE02207

Crank, J. (1975) *The Mathematics of Diffusion*. Oxford University Press, Oxford.

Dottin III, J.W., Labidi, J., Jackson, M.G., Farquhar, J. (2021) Sulfur isotope evidence for a geochemical zonation of the Samoan mantle plume. *Geochemistry, Geophysics, Geosystems* 22, e2021GC009816. https://doi.org/10.1029/2021GC009816

Dottin III, J.W., Farquhar, J., Labidi, J. (2018) Multiple sulfur isotopic composition of main group pallasites support genetic links to IIIAB iron meteorites. *Geochimica et Cosmochimica Acta* 224, 276–281. https://doi.org/10.1016/j.gca.2018.01.013

Gargano, A., Dottin, J., Hopkins, S.S., Sharp, Z., Shearer, C., *et al.* (2022) The Zn, S, and Cl isotope compositions of mare basalts: implications for the effects of eruption style and pressure on volatile element stable isotope fractionation on the Moon. *American Mineralogist*, in press. https://doi.org/10.2138/am-2022-8290

Heiken, G., McKay, D.S. (1974) Petrography of Apollo 17 soils. *Proceedings of the Fifth Lunar Conference* 1, 843–860. https://articles.adsabs.harvard.edu/pdf/1974LPSC....5..843H

Housley, R.M. (1978) Comments on the surface composition of lunar soil grains. *Earth and Planetary Science Letters* 41, 469–470. https://doi.org/10.1016/0012-821X(78)90178-4

McEwing, C.E., Thode, H.G., Rees, C.E. (1980) Sulphur isotope effects in the dissociation and evaporation of troilite: A possible mechanism for ^{34}S enrichment in lunar soils. *Geochimica et Cosmochimica Acta* 44, 565–571. https://doi.org/10.1016/0016-7037(80)90248-3

Rai, V.K., Jackson, T.L., Thiemens, M.H. (2005) Photochemical Mass-Independent Sulfur Isotopes in Achondritic Meteorites. *Science* 309, 1062–1065. https://doi.org/10.1126/science.1112954

Rees, C.E., Thode, H.G. (1974) Sulfur concentraitons of isotope ratios in Apollo 16 and 17 samples. *Proceedings of the Fifth Lunar Conference* 2, 1963–1973. https://articles.adsabs.harvard.edu/pdf/1974LPSC....5.1963R

Richter, F.M., Dauphas, N., Teng, F.-Z. (2009) Non-traditional fractionation of non-traditional isotopes: Evaporation, chemical diffusion and Soret diffusion. *Chemical Geology* 258, 92–103. https://doi.org/10.1016/j.chemgeo.2008.06.011

Saal, A.E., Hauri, E.H. (2021) Large sulfur isotope fractionation in lunar volcanic glasses reveals the magmatic differentiation and degassing of the Moon. *Science Advances* 7, abe4641. https://doi.org/10.1126/sciadv.abe4641

Schaefer, L., Lodders, K., Fegley Jr., B. (2012) Vaporization of the Earth: Application to exoplanet atmospheres. *The Astrophysical Journal* 755, 41. https://doi.org/10.1088/0004-637X/755/1/41

Switkowski, Z.E., Haff, P.K., Tombrello, T.A., Burnett, D.S. (1977) Mass fractionation of the lunar surface by solar wind sputtering. *Journal of Geophysical Research: Solid Earth and Planets* 82, 3797–3804. https://doi.org/10.1029/JB082i026p03797

Thode, H.G., Rees, C.E. (1971) Measurement of sulphur concentrations and the isotope ratios $^{33}S/^{32}S$, $^{34}S/^{32}S$ and $^{36}S/^{32}S$ in Apollo 12 samples. *Earth and Planetary Science Letters* 12, 434–438. https://doi.org/10.1016/0012-821X(71)90029-X

Thode, H.G., Rees, C.E. (1976) Sulphur isotopes in grain size fractions of lunar soils. *Proceedings of the Seventh Lunar Science Conference* 459–468. https://articles.adsabs.harvard.edu/pdf/1976LPSC....7..459T

Thode, H.G., Rees, C.E. (1979) Sulphur isotopes in lunar and meteorite samples. *Proceedings of the Tenth Lunar and Planetary Science Conference* 1629–1636. https://articles.adsabs.harvard.edu/pdf/1979LPSC...10.1629T

Wang, K., Moynier, F., Podosek, F.A., Foriel, J. (2012) An iron isotope perspective on the origin of the nanophase metallic iron in lunar regolith. *Earth and Planetary Science Letters* 337–338, 17–24. https://doi.org/10.1016/j.epsl.2012.05.021

Wing, B.A., Farquhar, J. (2015) Sulfur isotope homogeneity of lunar mare basalts. *Geochimica et Cosmochimica Acta* 170, 266–280. https://doi.org/10.1016/j.gca.2015.09.003

Wu, N., Farquhar, J., Dottin III, J.W., Magalhães, N. (2018) Sulfur isotope signatures of eucrites and diogenites. *Geochimica et Cosmochimica Acta* 233, 1–13. https://doi.org/10.1016/j.gca.2018.05.002

Zhang, Y. (2008) *Geochemical Kinetics*. Princeton University Press, Princeton.

Zhang, Y., Ni, H., Chen, Y. (2010) Diffusion Data in Silicate Melts. *Reviews in Mineralogy and Geochemistry* 72, 311–408. https://doi.org/10.2138/rmg.2010.72.8